Chapter 13
Identification of Dominant Modes for Cavitating Flows using Spectral Proper Orthogonal Decomposition

Grigorios Hatzissawidis, Moritz Sieber, and Peter F. Pelz

Abstract Cavitating flows exhibit complex, chaotic, multimodal, and intermittent behaviour. The dominant flow patterns are often hidden to the naked eye. Classical methods such as Proper Orthogonal Decomposition (POD) or Dynamic Mode Decomposition/Discrete Fourier Transformation (DMD/DFT) often fail to decompose the flow field into physically meaningful modes. To overcome this problem, we apply Spectral Proper Orthogonal Decomposition (SPOD). Using this method, it is possible to continuously shift between POD and DFT by varying a single parameter called filter size which is applied to the correlation matrix between individual snapshots. In this paper, SPOD is applied to high-speed images of cloud cavitation in the top and side view. We demonstrate that by appropriately varying the filter size, it is possible to decompose the data into the physical meaningful dominant modes. The intrinsic feature of SPOD to conduct a transient analysis through the time coefficients facilitates the understanding of the physical mechanisms corresponding to a specific mode. We show how the filter size affects the SPOD results and demonstrate how SPOD provides a more meaningful basis for modal representation of the images than POD and DMD/DFT. We perform a transient analysis to capture the intermittent flow behaviour, characterised by switching between two dominant modes as well as the presence of higher harmonics. Furthermore, extended SPOD (eSPOD) is applied to simultaneously captured pressure data along with the high-speed imaging, providing the correlation between the SPOD time coefficients and the pressure data.

Keywords Modal decomposition · Reduced-order modelling · Fluid mechanics · Cloud cavitation · Image processing

Introduction

Cloud cavitation is among the most severe forms of cavitation, commonly occurring in pumps, ship propellers, and mechanical heart valves [1]. It exhibits periodic behaviour, characterised by: (i) the formation and growth of a cavity sheet until it reaches an asymptotic length, (ii) the triggering of shedding by either re-entrant flow beneath the sheet, [2, 3], or an upstream-propagating condensation shockwave, [3, 4], and (iii) the formation of a cloud that is advected downstream due to the bulk flow. The subsequent collapse of this cloud may result in noise, vibration, erosion, efficiency drop etc.

The fundamental dynamics of cloud cavitation are not always immediately apparent to the naked eye. While it may appear unimodal, exhibiting a single shedding mode with a corresponding frequency, multimodal and intermittent behaviour can also occur, [5–7]. Multiple modes can occur simultaneously or exclusively. To gain deeper insights into the underlying physics, modal analysis tools have become increasingly prevalent in fluid mechanics problems [8]. These methods are typically applied to velocity fields obtained from simulations or Particle Image Velocimetry (PIV). However, in cavitation studies, experimental velocity fields are scarce, and high-speed imaging is more commonly employed. Consequently, modal analysis techniques are often applied to high-speed images to break down the flow field into physically meaningful modes.

Among these techniques, the most widely used are Proper Orthogonal Decomposition (POD), introduced by [9, 10], and Dynamic Mode Decomposition (DMD), introduced by [11]. POD ranks modes based on their variance, which corresponds to the turbulent kinetic energy when the snapshots represent velocity fields. DMD generates modes that are characterised by distinct frequencies and associated growth or decay rates.

Grigorios Hatzissawidis · Peter F. Pelz
Chair of Fluid Systems, Technische Universität Darmstadt, 64287 Darmstadt, Germany
e-mail: grigorios.hatzissawidis@tu-darmstadt.de; peter.pelz@tu-darmstadt.de

Moritz Sieber
Laboratory for Flow Instabilities and Dynamics, Technische Universität Berlin, 10623 Berlin, Germany
e-mail: m.sieber@fdx.de

Brandon Dilworth et al. (eds.), *Topics in Modal Analysis & Parameter Identification I, Vol. 9*, Conference Proceedings of the Society for Experimental Mechanics Series, https://doi.org/10.13052/97887-438-0154-2_13

However, these methods have certain limitations: POD modes may not clearly decompose specific underlying physical phenomena, as the dynamics of different modes can be mixed, i.e., the temporal coefficients contain more than one frequency. In contrast, DMD assigns a single frequency to each mode, which does not account for subtle cycle-to-cycle variations. If the frequency undergoes slight changes, the mode shifts to neighbouring frequencies, limiting the method's ability to capture gradual frequency variations. Moreover, determining which modes hold physical significance is challenging, as DMD does not inherently provide a ranking of modes. To address these challenges, Spectral Proper Orthogonal Decomposition (SPOD) is used [12, 13]. This method enables a continuous transition between POD and DFT by applying a filter to the correlation matrix of individual snapshots, thereby providing a more flexible decomposition. The only parameter that requires adjustment is the filter size, which must be carefully selected based on the specifics of the underlying problem. The intrinsic capability of SPOD to perform transient analysis through its time coefficients is crucial for data analysis, as modes in cavitating flows may occur intermittently.

To demonstrate the method, we apply SPOD to high-speed images of cloud cavitation. We extend our study in [13], conducting a more detailed analysis. Specifically, we examine the impact of filter size and illustrate how two distinct physical modes can be decomposed. Following this, a transient analysis is conducted, revealing that the modes occur exclusively and providing evidence of higher harmonics. Finally, we employ extended SPOD (eSPOD), [14, 15], allowing us to correlate data from other sources with the SPOD results.

Experimental overview

Experiments were performed at the water cavitation tunnel at the Technische Universität Darmstadt. The test section has a rectangular cross-sectional area with a height H of $70\,\mathrm{mm}$, a depth b of $25\,\mathrm{mm}$, and a length of $462\,\mathrm{mm}$. The test model is a two-dimensional NACA0015 hydrofoil having a chord length L of $46\,\mathrm{mm}$, positioned along the centreline of the test section and spanning its full depth. A schematic view of the test section is provided in Figure 1. For more details regarding the test rig, we refer to [13]. The data used in this study is the same as in [13]. The operation point is defined with the chord-based Reynolds number, $Re \coloneqq U_\infty\, L/\nu$, and the cavitation number $\sigma \coloneqq 2\,(p_\infty - p_\mathrm{v})\,/\left(\varrho U_\infty^2\right)$, where U_∞ and p_∞ represents the reference free-stream velocity and pressure and p_v, ϱ and ν denote the fluid's vapour pressure, density and kinematic viscosity, respectively.

The experiment in this study is performed at a fixed Reynolds number of $Re = 8\times10^5$, a cavitation number of $\sigma = 2$ and an incidence α of $12°$. This operating point was selected because it exhibits intermittent and multimodal behaviour, making it suitable for the analysis of complex cavitation dynamics. All uncertainties were quantified in accordance with the ISO Guide to the Expression of Uncertainty in Measurement (GUM), [16]. To characterise the inflow, Laser Doppler Velocimetry (LDV) measurements were performed. The flow uniformity was found to deviate by no more than 3% at its maximum, [13]. High-speed imaging was conducted using a dual-camera system, consisting of a Photron FASTCAM NOVA S12 for the top view and an IDT MotionPro Y7 S3 for the side view. Both cameras operated at a frame rate of $18\,\mathrm{kHz}$, with spatial resolutions of $0.078\,\mathrm{mm/px}$ and $0.035\,\mathrm{mm/px}$ using a Carl Zeiss Makro-Planar T* 2/50 mm ZF lens and Carl Zeiss Distagon 1.4/35 mm lens, respectively. Illumination was provided by two triggered Veritas Constellation 120 LED lights and one IDT 19-LED.

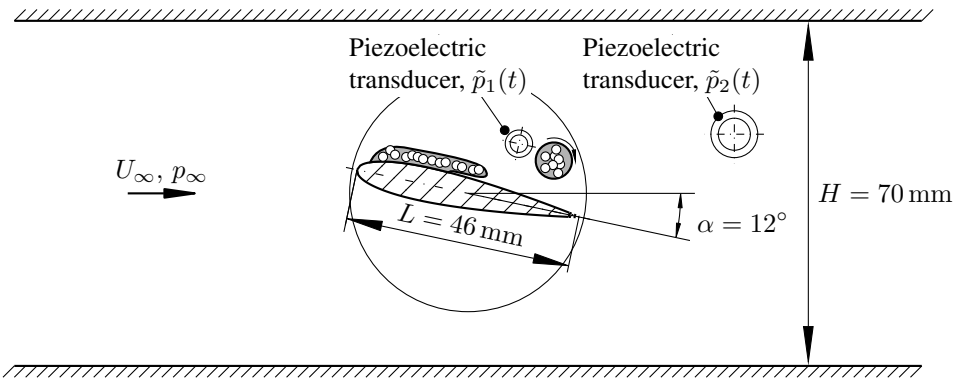

Fig. 1 A schematic representation of the hydrofoil within the test section is shown. The model is a two-dimensional NACA0015 hydrofoil with a chord length of $46\,\mathrm{mm}$ and a span of $25\,\mathrm{mm}$. A cavity sheet forms near the hydrofoil's leading edge and periodically sheds cavitation clouds. The flow direction is from left to right.

Unsteady pressure measurements were simultaneously acquired using two piezoelectric transducers: a Kistler type 601CAB with an eigenfrequency of 215 kHz, and a Kistler type 701A with an eigenfrequency of 70 kHz, both connected to Kistler 5018A single-channel charge amplifiers, cf. Figure 1. The first transducer is flush-mounted 8 mm downstream and 8 mm above the rotational axis of the hydrofoil and rotates along with it. The second transducer is flush-mounted 54 mm downstream and 12 mm above the rotational axis. The recorded pressure signals are denoted as $\tilde{p}_1(t)$ and $\tilde{p}_2(t)$, respectively.

Modal analysis using SPOD and extended SPOD

Spectral Proper Orthogonal Decomposition, developed by Sieber et al. [12], is applied to the time-varying pixel intensities $I(\mathbf{x}, t)$ of high-speed images to extract the dominant coherent structures in cloud cavitation and their corresponding frequencies as it is conducted in [13]. The following provides a brief overview of the SPOD calculation, while a detailed description of the SPOD algorithm can be found in [12]. The procedure follows the method of snapshots approach [10]. We seperate our data into a mean and fluctuating components, $I(\mathbf{x}, t) = \overline{I}(\mathbf{x}) + I'(\mathbf{x}, t)$ and decompose only the fluctuating part into N SPOD spatial modes $\Psi_i(\mathbf{x})$ and temporal coefficients $b_i(t)$:

$$I'(\mathbf{x}, t) = \sum_{i=1}^{N} b_i(t)\Psi_i(\mathbf{x}), \tag{1}$$

where N is the number of time-resolved snapshots. The core concept of SPOD involves applying a filter to the correlation matrix of the individual snapshots $R_{i,j} = 1/N \langle I'(\mathbf{x}, t_i), I'(\mathbf{x}, t_j)\rangle$. The eigendecomposition of the filtered correlation matrix $\mathbf{S}$ yields the temporal coefficients $\mathbf{b}_i$ and the corresponding mode energies μ_i through the eigenvalue decomposition $\mathbf{S}\mathbf{b}_i = \mu_i \mathbf{b}_i$. To clarify, the mode energies in the case of intensity values do not represent physical energies; rather, they correspond to variances in a more general sense. The spatial modes are obtained by projecting the snapshots onto the temporal coefficients, cf. [12]. Once the modes are identified, it is necessary to establish mode pairs, similar to the sine and cosine components in the Fourier Transform, [13]. This pairing is achieved by evaluating the harmonic correlation between individual modes.

The key parameter of SPOD to be adjusted is the filter size N_f. For no filter or $N_\mathrm{f} = 0$, the method simplifies to the classic POD. When the filter encompasses the entire correlation matrix or $N_\mathrm{f} = N$, we obtain a DFT. While a true DFT corresponds to an infinite filter size, the outcome remains nearly unchanged for $N_\mathrm{f} > N$. The filter size must be tailored to the underlying problem. An appropriate filter size is achieved when the results remain stable and unaffected by variations around the selected filter size.

The primary advantage of SPOD lies in its inherent capability to perform transient analysis using the time coefficients. From the complex time coefficients $\tilde{b}_i(t) = b_j(t) + \mathrm{i}\, b_k(t)$, where the time coefficients j and k constitute mode i and are identified through the harmonic correlation, both amplitude and phase can be extracted, $\tilde{b}_i(t) = |\tilde{b}_i(t)| \exp[\mathrm{i}\,\varphi(t)]$. The derivative of the phase $\partial\varphi(t)/\partial t$ equals the time-resolved angular frequency $\omega(t)$, where the frequency in Hz can be calculated as $f(t) = \omega(t)/(2\pi)$ and the Strouhal number as $St(t) = f(t)\, L/U_\infty$, enabling a detailed frequency-time analysis.

We applied the extended POD (ePOD), once again utilising the time coefficients. Originally introduced by Borée, [14], for classical POD, ePOD can be seamlessly extended to SPOD through the use of its time coefficients, a method referred to as extended SPOD, cf. [15]. eSPOD enables the modal representation of additional quantities that are recorded simultaneously with the decomposed data or snapshots. It is possible to use entire fields, such as pressure fields or intensities of OH*-chemiluminescence, as demonstrated in [15, 17]. In this study, we employ the two unsteady one-dimensional pressure signals from the two piezo-electric transducers, Figure 1. The formulation of eSPOD is analogous to the Pearson correlation coefficient between the ith complex time coefficient $\tilde{b}_i(t)$ and the unsteady pressure signal $\tilde{p}_k(t)$, expressed as

$$r_{\tilde{b}_i(t),\tilde{p}_k(t)} \coloneqq \frac{1}{N\,\sigma\left[\tilde{b}_i(t)\right]\sigma[\tilde{p}'_k(t)]} \sum_{j=1}^{N} \tilde{b}_i(t_j)\,\tilde{p}'_k(t_j), \tag{2}$$

with $\tilde{p}'_k(t)$ being the fluctuating part of $\tilde{p}_k(t)$, $k = 1, 2$. The absolute value of the complex Pearson correlation coefficient can range between 0 and 1, indicating no correlation and perfect correlation, respectively.

In the present study, a total of $N = 8001$ high-speed images are used and downscaled to 50% of their original size. A mask is applied to cover the location of the piezoelectric transducer and the hydrofoil in the side view. The image edges are handled by applying periodic boundary conditions.

Results & Discussion

The SPOD spectrum for a filter size N_f of 300, corresponding to 3.58 periods of the first mode with $f_1 = 215\,\mathrm{Hz}$ or $St_1 = 0.61$, is shown Figure 2. The Power Spectral Density (PSD) calculated using the Welch method, [18], of the unsteady pressure signals $\tilde{p}_1$ and $\tilde{p}_2$, is also included in the same spectrogram for comparison. The two peaks extracted from these signals are indicated by vertical dotted lines in the spectrogram, corresponding to $St_1 = 0.61,\ St_2 = 0.14$ or $f_1 = 215\,\mathrm{Hz},\ f_2 = 50\,\mathrm{Hz}$. The first two modes identified by the SPOD correspond to these two frequency peaks. The blade pass frequency of the main pump is also represented as a vertical line in the spectrogram. The SPOD spectrum from the high-speed images does not reveal any modes at this frequency, indicating that no fluctuations at the blade-pass frequency are influencing the cavitation behaviour.

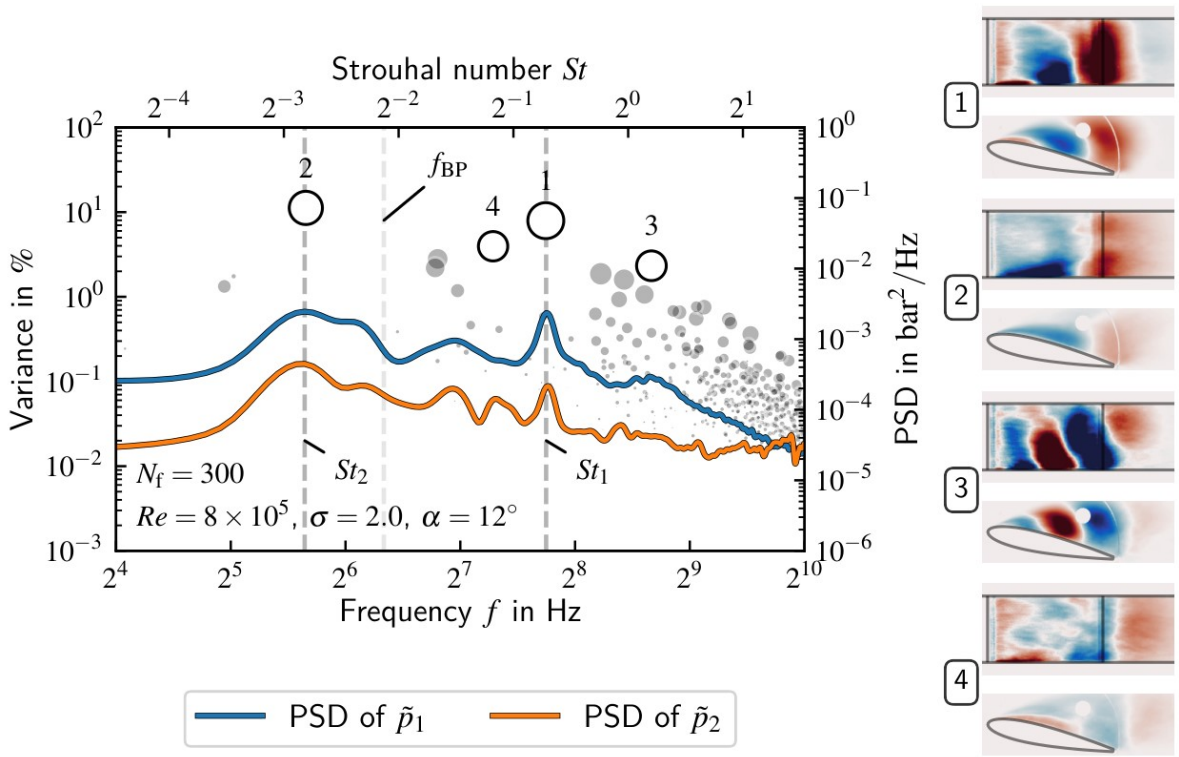

Fig. 2 SPOD spectrum for a filter size of $N_\mathrm{f} = 300$. The modes are organized according to their harmonic correlation, which is visually represented by the size of the dots. The first four modes are highlighted. The frequencies St_1 and St_2, corresponding to the two dominant peaks extracted from the piezoelectric transducer, align with the first two dominant modes identified by SPOD. At the right-hand side, the real part of the first four spatial modes in the side and top view are plotted.

At the right-hand side, the real parts of the four spatial modes Ψ_i are plotted. Mode 1 has a slightly smaller wavelength in the flow direction than mode 2. These modes correspond to the periodic cloud cavitation occurring at higher and lower frequencies, respectively. Mode 3 has a smaller wavelength than Modes 1 and 2 and approximately double the frequency of Mode 1, with $f_3 = 406\,\mathrm{Hz}$ or $St_3 = 1.15$. It contains components of higher harmonics of Mode 1, as will be shown later. It is not obvious which physical, coherent structure mode 3 corresponds to, although this frequency is prominent in the PSD of $\tilde{p}_2$, while it is absent in $\tilde{p}_1$.

The influence of the filter size on the identification of the dominant modes is shown, Figure 3. The horizontal lines for St_1 and St_2 are the frequencies extracted from the PSD from pressure signals $\tilde{p}_1$ and $\tilde{p}_2$. As the filter size N_f increases, the relative variance (or energy, in the case of a velocity field) decreases, which is denoted by the size of the dot. It is distributed across additional weaker modes, thereby increasing the noise component. An appropriate filter size is one where the decomposition remains stable and does not strongly depend on slight variations in the filter size. We find that a filter size of $N_\mathrm{f} = 300$ is suitable, as it captures the dominant features without losing too much variance. This dependency is also discussed in [19]. It is noteworthy that, depending on the filter size, the ordering of the modes – based on harmonic correlation – varies.

It can also be observed that with smaller filter sizes, approaching the behaviour of POD, the mode with the frequency St_1 is not detected. On the other hand, in the extreme case approaching the DFT, the two peaks detected align with St_1 and St_2; however, the other modes become indistinct, and the variance is dispersed into weaker, less significant modes.

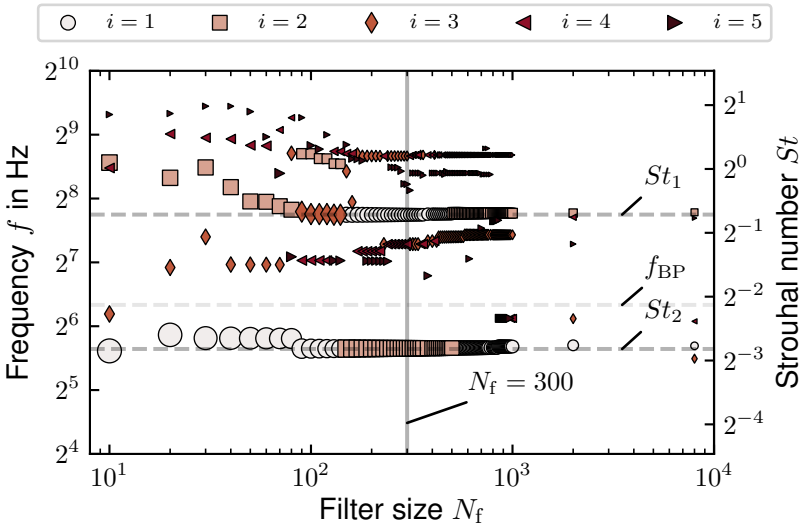

Fig. 3 The frequencies of the identified ith modes are plotted against the filter size N_f. The size of the dots represents the relative variance of the individual modes, decreasing with higher filter size. The vertical line denotes the filter size at 300 which was selected for further analysis. The horizontal lines represent the frequencies extracted from the PSD of the pressure signals. The blade pass frequency is also plotted, demonstrating that no modes are identified at this frequency for any filter size.

This behaviour becomes more evident when examining the PSD of the time coefficients across different filter sizes, cf. Figure 4. For a sensible comparison, we take the modes for each filter size, which corresponds to the frequency St_1 and St_2, respectively. Again, the vertical lines are the frequencies from the peaks of the piezoelectric transducers. Figure 4 (a) illustrates the filter coefficients associated with St_1, while Figure 4 (b) presents those corresponding to St_2. With a filter size of 50, the two modes are not distinctly separated, as evidenced by the two broad peaks around St_1 and St_2. Consequently, the dynamics of these modes become intertwined. As the filter size increases to 400, the peaks become narrower, while the spectral content diminishes at higher frequencies in Figure 4 (b) and at both lower and higher frequencies in Figure 4 (a). An effective approach for selecting the appropriate filter size is to choose the smallest value at which no spectral content from other flow structures is apparent in the spectrum, [20]. For a filter size of 300, this condition is satisfied, keeping in mind that the scale is logarithmic. In the DFT case, with $N_f = 8001$, the peaks are well identified; however, the variance is dispersed across other frequencies, and variations in both frequency and amplitude cannot be detected.

In contrast, SPOD is well-suited for transient analysis. The real and complex components of the time coefficients for modes 1 and 2 are shown in Figure 5. Figure 5 (a) to (d) reveals that the modes are not consistently present over time. Between $t' = 100$ and 140, mode 2 becomes dominant, while mode 1 weakens, indicating that these modes occur exclusively. This variation in amplitude demonstrates that the modes occur intermittently. The Probability Density Function (PDF) of the Strouhal number at the right hand side of Figure 5 (b) and (d) shows the slight modulation in frequency. The corresponding amplitude-weighted mean and standard deviation is also given.

The tendency of the modes 1 and 2 to occur exclusively becomes particularly evident when plotting the real part of the time coefficient of mode 1, $\Re(\tilde{b}_1)$, against the absolute value of the time coefficient of mode 2, $|\tilde{b}_2|$, as shown in Figure 6. When mode 2 is weak, indicated by a low amplitude $|\tilde{b}_2|$, mode 1 exhibits strong fluctuations, as reflected by the real part of the time coefficient $\Re(\tilde{b}_1)$. These fluctuations tend to diminish as $|\tilde{b}_2|$ increases.

We now analyse the correlation between mode 1 and mode 3. Given that the latter has approximately half the wavelength, as shown in Figure 2, and exhibits twice the frequency, with $St_1 = 0.61$ and $St_3 = 1.15$, this suggests that mode 3 could be a harmonic of mode 1. The Lissajous figure, real part of the time coefficient $\tilde{b}_1$ against the real part of the time coefficient $\tilde{b}_3$, exhibit an eight-shape, indicating that there is a phase relation between mode 1 and 3, see Figure 7 (b). However, without the red averaged curve over the cycles, this relationship would not be immediately apparent to the unaided eye. For completeness, the real and imaginary parts of $\tilde{b}_1$ are plotted to illustrate the shrinking and growing cycles, highlighting the intermittent behaviour of mode 1, see Figure 7 (a).

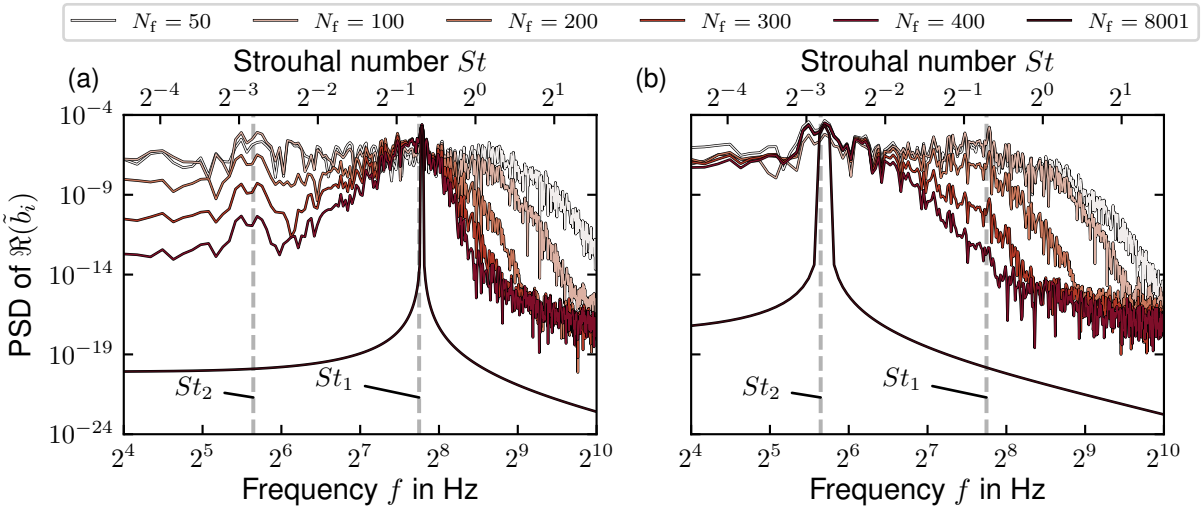

Fig. 4 The PSD of the real part of the time coefficients for varying filter size. For a sensible comparison, the modes corresponding to St_1 and St_2 from the piezoelectric transducers are taken, since the order of the modes for varying filter sizes changes.

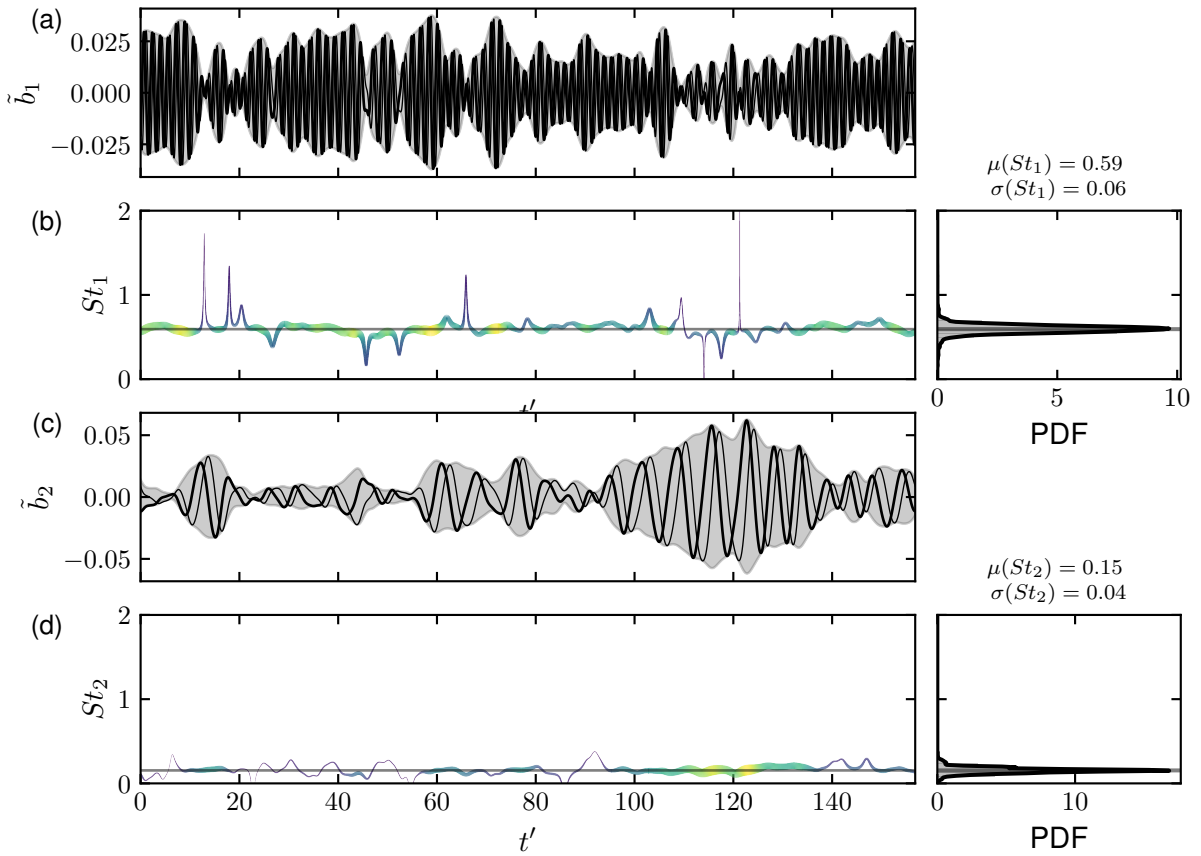

Fig. 5 (a) and (c) Complex time coefficients for mode 1 and 2 for a filter size of $N_f = 300$ and (b) and (d) the Strouhal numbers for mode 1 and 2 over time calculated from the complex time coefficients, respectively. The colourmap indicates the absolute value or the amplitude. The grey-filled area is the envelope of the real and complex part of the time coefficient, which equals the amplitude. The Probability Density Function (PDF) is calculated from the time-varying Strouhal number. $\mu(St_i)$ and $\sigma(St_i)$ are the weighted mean and the weighted standard deviation, respectively.

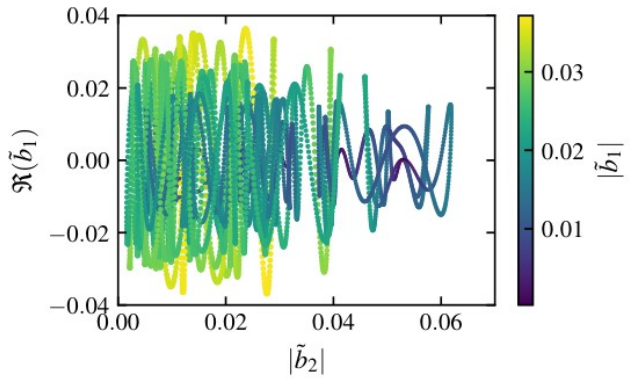

Fig. 6 The real part of the time coefficient of mode 1, $\Re(\tilde{b}_1)$, plotted against the absolute value of the time coefficient of mode 2, $|\tilde{b}_2|$, highlights their intermittent behaviour. The colourbar represents the absolute value of $|\tilde{b}_1|$ to enhance visualisation.

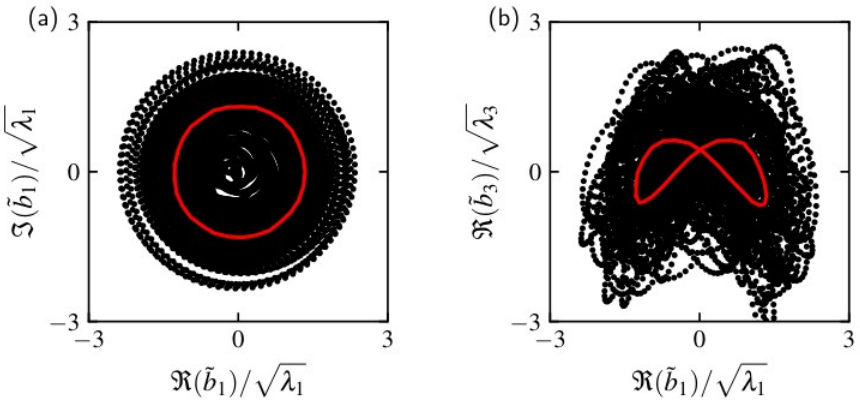

Fig. 7 The Lissajous figure of the real part of the time coefficient $\tilde{b}_1$ for mode 1 is plotted against (a) its imaginary part, and (b) the real part of the time coefficient $\tilde{b}_3$ for mode 3. The time coefficients are normalised by their variance. The red lines are the phase-average over the cycles.

Further analysis following the procedure in [20] confirms that modes 3 is a harmonic of mode 1. We plot the phase angles of mode 1 and mode 3, $\varphi_1 = \arg(\tilde{b}_1)$ and $\varphi_3 = \arg(\tilde{b}_3)$, respectively, against each other in Figure 8 (a), and display the histogram of the phase difference $2\varphi_1 - \varphi_3$ as a density plot in Figure 8 (b). Since these modes are harmonics, the phase angle dots for φ_1 and φ_3 are arranged along three primary diagonals, as seen in Figure 8 (b), and the histogram

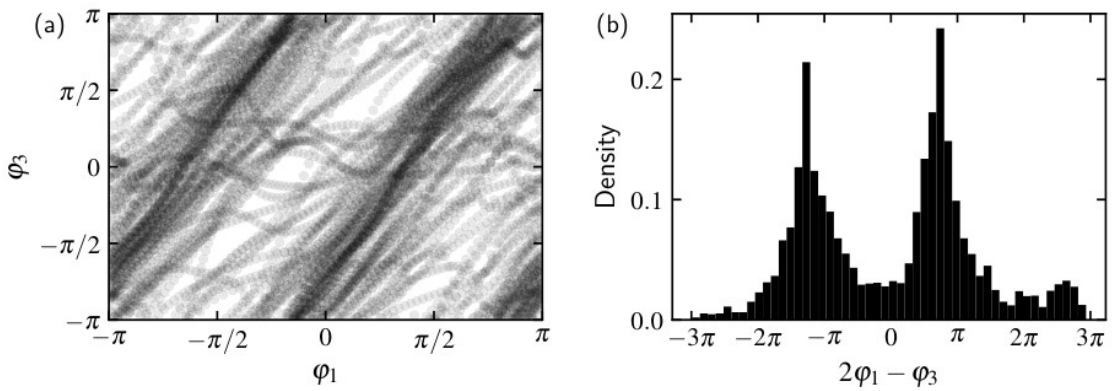

Fig. 8 Correlation between the phase angle of mode 1 and mode 3. (a) Phase angle φ_3 against φ_1, (b) histogram of the phase difference between mode 1 and 3.

exhibits distinct peaks, indicating a clear phase relationship between the two modes. Given that this trend is not consistently observed, it can be concluded that modes 1 and 3 are not perfectly coupled. It is possible that the harmonic lags behind or exhibits an ill-defined phase difference. Due to the highly transient nature of the flow, the coupling between these modes remains weak.

We proceed by applying extended SPOD (eSPOD) using the pressure data from the piezoelectric transducers. The correlation, as defined in eq. (2), between the time coefficients of modes 1 to 10 and $\tilde{p}_1$ and $\tilde{p}_2$ is shown in Figure 9 (a) and Figure 9 (b), respectively. Since the high-speed imaging is conducted at a lower frequency than the pressure measurements, the time coefficients must be upscaled accordingly. The pressure signal $\tilde{p}_1$ shows a stronger correlation with the time coefficient of mode 2, $\tilde{b}_2$, compared to its correlation with $\tilde{p}_2$. To visualise this, we plot the time curve of $\Re(\tilde{b}_2)$ alongside $\tilde{p}_1$, where mode 2 exhibits a strong presence, as indicated by a high amplitude $|\tilde{b}_2|$, specifically in the range $t' = 90$ to 150, as shown in Figure 10. The prime symbol $(\cdot)'$ in Figure 10 denotes that a signal $y(t)$ is normalised according to $[y(t)]' = \{y(t) - \mu[y(t)]\}/\sigma[y(t)]$, where μ and σ represent the mean value and standard deviation, respectively. Dividing the complex time coefficient of mode 2, $\tilde{b}_2$, by the Pearson correlation coefficient $r_{\tilde{b}_2,\tilde{p}_1}$, yields the phase-shifted time coefficient, as illustrated by the blue line in Figure 10 (a). It becomes evident that the time coefficient closely follows the same trend as the pressure signal.

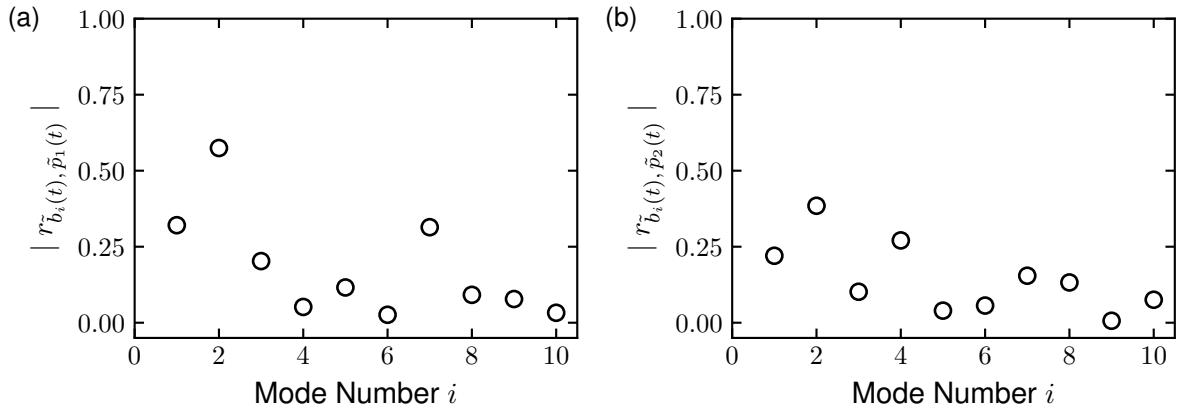

Fig. 9 Results of the eSPOD. The absolute value of Pearson correlation coefficient between the time coefficients and (a) the pressure data $\tilde{p}_1(t)$ and (b) the pressure data $\tilde{p}_2(t)$.

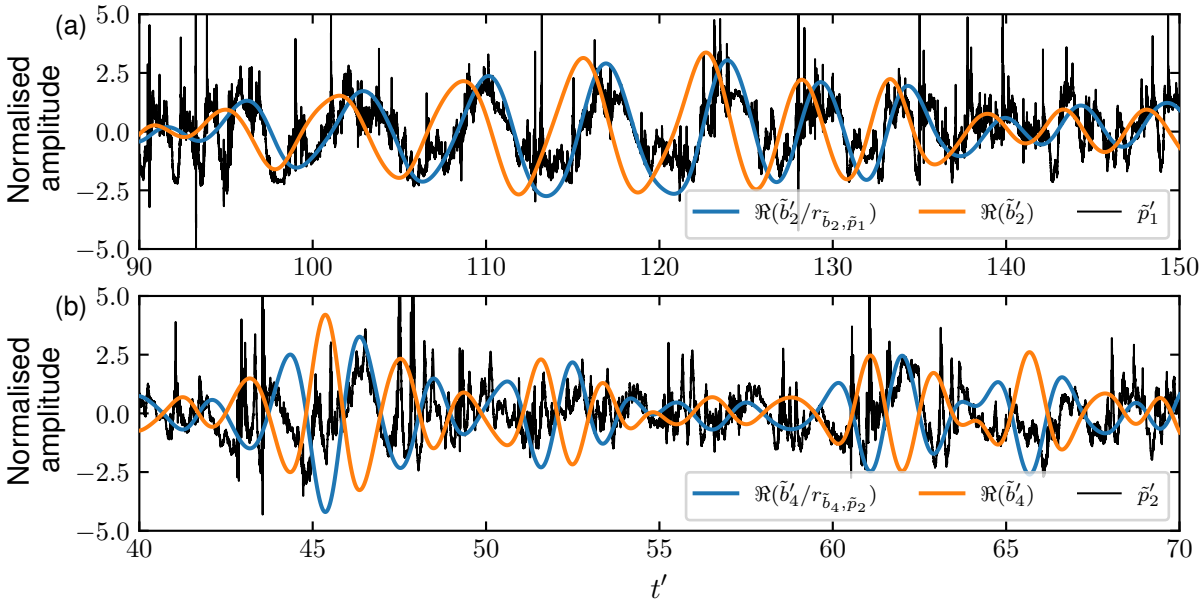

Fig. 10 The pressure signal and the real part of the time coefficient, as well as the phase-shifted time coefficient using Pearson correlation coefficient for (a) mode 2 and $\tilde{p}_1$, and (b) mode 4 and $\tilde{p}_2$. It is evident that the time coefficient follows the trend of the pressure signals.

Applying the same procedure using the time coefficient of mode 4, $\tilde{b}_4$, and $\tilde{p}_2$, we observe that mode 4 follows the trend of $\tilde{p}_2$. However, mode 4 alone is insufficient to fully reconstruct the signal. The results from the eSPOD analysis are consistent with the observations from the SPOD spectrogram and the pressure data's PSD, as shown in Figure 2. The frequency at which mode 4 appears is not evident in $\tilde{p}_1$ but is clearly visible in $\tilde{p}_2$, explaining the stronger correlation of $\tilde{b}_4$ with $\tilde{p}_2$ rather than with $\tilde{p}_1$. It should be noted that the high-frequency components, observed in the pressure signals as peaks and rapid variations, cannot be reconstructed using the time coefficients, as the high-speed data are recorded at a lower sampling frequency. These peaks are caused by condensation shocks occurring during cavitation. However, the low-frequency variations, such as cloud shedding, can still be detected.

Conclusions

Spectral Proper Orthogonal Decomposition was applied to decompose time-resolved high-speed images and identify the dominant coherent spatial structures and their corresponding frequencies. The chosen operating point exhibited intermittent and multi-modal behaviour. SPOD successfully identified the two dominant shedding modes from the high-speed recordings, whereas classical methods like POD and DFT failed. We demonstrated this by varying the filter size, allowing a continuous transition between POD and DFT. Setting the filter size appropriately is crucial, as it requires balancing the loss of variance (or turbulent kinetic energy in the case of velocity data) with the need to effectively decompose individual physical modes.

A key advantage of SPOD is its ability to conduct transient analysis, unlike other methods that require more data to capture the dominant structures. SPOD is particularly well-suited for transient analysis, as it does not demand large datasets but rather requires the inclusion of relevant dynamics. The transient analysis revealed that the two dominant modes, with higher and lower frequencies, $St_1 = 0.61$ and $St_2 = 0.14$, occur exclusively. This was further validated by examining the time coefficients and plotting them against each other. Additionally, a high-frequency mode 3 was identified as a higher harmonic of mode 1 through the use of Lissajous figures and phase analysis.

We further applied extended SPOD to incorporate pressure data from two piezoelectric transducers. This allowed for the modal representation of additional quantities that were recorded simultaneously with the decomposed data, equivalent to the Pearson correlation coefficient. It was evident from the time curves that, when strong correlations exist between the pressure data and the time coefficients, their trends closely follow each other.

Both SPOD and eSPOD provide a robust framework for physically meaningful data decomposition, aiding in the understanding of the underlying physical mechanisms.

Acknowledgments We kindly acknowledge the financial support by the Deutsche Forschungsgemeinschaft (DFG, German Research Foundation) —Project-ID 265191195—Collaborative Research Center 1194 (CRC 1194) "Interaction between Transport and Wetting Processes", project C06. The authors also gratefully acknowledge the support of the Federal Ministry for Economic Affairs and Climate Action (BMWK). The authors also thank Mr Udo Trometer and Mr Andreas Schuler for the technical support and manufacturing of the specimens.

References

1. Lee, H. and Taenaka, Y. "Characteristics of Mechanical Heart Valve Cavitation in a Pneumatic Ventricular Assist Device". *Artificial Organs*, 32(6):453–460 (2008).
2. Pelz, P.F., Keil, T., and Groß, T.F. "The transition from sheet to cloud cavitation". *Journal of Fluid Mechanics*, 817:439–454 (2017).
3. Hatzissawidis, G., Kuhr, M.M., and Pelz, P.F. "The transition from re-entrant flow-driven to shockwave-driven cloud cavitation". *Journal of Fluid Mechanics*, 1004:A13 (2025).
4. Ganesh, H., Mäkiharju, S.A., and Ceccio, S.L. "Bubbly shock propagation as a mechanism of shedding in separated cavitating flows". *Journal of Hydrodynamics, Ser. B*, 29(6):907–916 (2017).
5. Wu, J., Ganesh, H., and Ceccio, S. "Multimodal partial cavity shedding on a two-dimensional hydrofoil and its relation to the presence of bubbly shocks". *Experiments in Fluids*, 60(4):66 (2019).
6. Smith, S.M., Venning, J.A., Pearce, B.W., Young, Y.L., and Brandner, P.A. "The influence of fluid–structure interaction on cloud cavitation about a stiff hydrofoil. Part 1.". *Journal of Fluid Mechanics*, 896:A1 (2020).
7. Venning, J.A., Pearce, B.W., and Brandner, P.A. "Nucleation effects on cloud cavitation about a hydrofoil". *Journal of Fluid Mechanics*, 947:A1 (2022).
8. Taira, K., Brunton, S.L., Dawson, S.T., Rowley, C.W., Colonius, T., McKeon, B.J., Schmidt, O.T., Gordeyev, S., Theofilis, V., and Ukeiley, L.S. "Modal analysis of fluid flows: An overview". *AIAA Journal*, 55(12):4013–4041 (2017).
9. Lumley, J.L. *Stochastic Tools in Turbulence*. Academic Press (1970).
10. Sirovich, L. "Turbulence and the dynamics of coherent structures. I. Coherent structures". *Quarterly of Applied Mathematics*, 45(3):561–571 (1987).

11. Schmid, P.J. “Dynamic mode decomposition of numerical and experimental data”. *Journal of Fluid Mechanics*, 656:5–28 (2010).
12. Sieber, M., Paschereit, C.O., and Oberleithner, K. “Spectral proper orthogonal decomposition”. *Journal of Fluid Mechanics*, 792:798–828 (2016).
13. Hatzissawidis, G., Sieber, M., Oberleithner, K., and Pelz, P.F. “Data-driven spatiotemporal analysis of cloud cavitation by means of spectral proper orthogonal decomposition”. *Experiments in Fluids*, 66(5):104 (2025).
14. Borée, J. “Extended proper orthogonal decomposition: A tool to analyse correlated events in turbulent flows”. *Experiments in Fluids*, 35(2):188–192 (2003).
15. Sieber, M., Paschereit, C.O., and Oberleithner, K. “Advanced Identification of Coherent Structures in Swirl-Stabilized Combustors”. *Journal of Engineering for Gas Turbines and Power*, 139(2):021503 (2017).
16. International Organization for Standardization. “ISO/IEC Guide 98-3:2008: Uncertainty of measurement – Part 3: Guide to the expression of uncertainty in measurement (GUM:1995)” (2008).
17. Verdoya, J., Dellacasagrande, M., Lengani, D., Simoni, D., and Ubaldi, M. “Inspection of structures interaction in laminar separation bubbles with extended proper orthogonal decomposition applied to multi-plane particle image velocimetry data”. *Physics of Fluids*, 33(4):043607 (2021).
18. Welch, P.D. “The Use of Fast Fourier Transform for the Estimation of Power Spectra: A Method Based on Time Averaging Over Short, Modified Periodograms”. *IEEE Transactions on Audio and Electroacoustics*, 15(2):70–73 (1967).
19. Mohammadi, A., Morton, C., and Martinuzzi, R.J. “Benefits of FIR-based spectral proper orthogonal decomposition in separation of flow dynamics in the wake of a cantilevered square cylinder”. *International Journal of Heat and Fluid Flow*, 104:109224 (2023).
20. Vanierschot, M., Muller, J.S., Sieber, M., Percin, M., Van Oudheusden, B.W., and Oberleithner, K. “Single- and double-helix vortex breakdown as two dominant global modes in turbulent swirling jet flow”. *Journal of Fluid Mechanics*, 883:A31 (2020).